Accurate first principles band gap predictions in strain engineered ternary III-V semiconductors

Badal Mondal●

Wilhelm-Ostwald-Institut für Physikalische und Theoretische Chemie, Universität Leipzig, 04103 Leipzig, Germany
and Fachbereich Physik, Philipps-Universität Marburg, 35032 Marburg, Germany

Marcel Kröner, Thilo Hepp●, and Kerstin Volz●

Material Science Center and Department of Physics, Philipps-Universität Marburg, D-35043 Marburg, Germany

Ralf Tonner-Zech●*

Wilhelm-Ostwald-Institut für Physikalische und Theoretische Chemie, Universität Leipzig, 04103 Leipzig, Germany

Tuning the band gap in ternary III-V semiconductors via modification of the composition or the strain in the material is a major approach for the design of optoelectronic materials. Experimental approaches screening a large range of possible target structures are hampered by the tremendous effort to optimize the material synthesis for every target structure. We present an approach based on density functional theory efficiently capable of providing the band gap as a function of composition and strain. Using a specific density functional designed for accurate band gap computation (TB09) together with a band unfolding procedure and special quasirandom structures, we develop a computational protocol to predict band gaps. The approach's accuracy is validated by comparison to selected experimental data. We thus map the band gap over the phase space of composition and strain (we call this the "band gap phase diagram") for several important III-V compound semiconductors: GaAsP, GaAsN, GaPSb, GaAsSb, GaPBi, and GaAsBi. We show the application of these diagrams for identifying the most promising materials for device design. Furthermore, our computational protocol can easily be generalized to explore the vast chemical space of III-V materials with all other possible combinations of III and V elements.

I. INTRODUCTION

Materials based on III-V semiconductor compounds are attracting much attention in science and engineering due to their diverse applications in fields such as optoelectronics [1,2]. One of the main goals of basic and applied research is to tailor materials' optical properties to a specific application [3–8]. One of the most critical fundamental properties in this respect is the band gap, both in terms of size and type (direct or indirect). For example, optical telecommunication applications require materials with direct band gaps in the range of 0.80–0.95 eV [3–5], while solar cell applications require a range of 0.5–2.0 eV [6–8]. Composition engineering, i.e., changing the relative composition of group 13 and 15 elements in ternary III-V compounds, is one of the most important approaches to adjusting the band gap [9–22]. Systematic application of strain such as mechanical strain (e.g., external pressure [23–26], mechanical bending of nanowires [27–29]) or strain due to lattice mismatch (e.g., core-shell mismatch in nanowires [30–34]) on a system are alternative strategies to tailor the band gap. Combining composition and strain engineering, the band gap can be tuned over a wide range of values, and direct or indirect semiconductors can be designed. In thin-layer heteroepitaxy, choosing the substrate-layer

combination with minimum lattice mismatch is often desirable to minimize the strain effect from the substrate. However, in practice, perfect lattice matching is rarely possible. In such cases, not only the composition but the effect of inherent strain from the substrate also substantially affects the active layer's band gap [9–22,35–39]. Therefore, one requires a complete knowledge of the material-specific dependence of the band gap on composition and strain to guide the optimal choice of materials. However, exploring the vast chemical space of all possible combinations of III and V elements with variation in composition and strain is experimentally not feasible. Additionally, growing a new material is often challenging because of thermodynamic or kinetic limitations, such as phase separation or surface roughening, in addition to the demanding task of optimizing the growth conditions [9,13,16,19,21,22]. This makes an experimental screening approach of vast compound and strain spaces unrealistic. We thus aim in this study to develop a reliable and predictive theoretical approach.

Two major theoretical approaches that have been used to analyze strain effects on the band gap of III-V materials are (semi-)empirical methods and *ab initio* approaches. Although (semi-)empirical methods such as $k \cdot p$ theory [36,40] and tight-binding methods [36,41–43] are computationally efficient, they rely on empirical parameters which require system-specific experimental input data. This strongly limits the predictive ability of these methods for new or yet unknown materials. Additionally, in case of a large

*ralf.tonner@uni-leipzig.de

mismatch in atomic sizes of the constituting elements, the ternary material shows local strain effects, severely affecting the band gap [44]. These local strain effects, however, can not be included in empirical approaches and, hence, are neglected. Then again, *ab initio* approaches such as density functional theory (DFT) [40,45–50] allow for the calculation of electronic properties from first principles and are thus predictive if accurate density functional are used. The relaxation of the atomic positions also allows to properly include and investigate the effect of the local strain on the electronic properties in these approaches. Additionally, recent advancements in the modeling strategies of alloy systems using quasirandom supercells [51–55] allow for electronic properties calculations in the *ab initio* approaches, even for diluted and disordered materials. An accurate alternative to DFT approaches is the use of GW-based methods, which are nevertheless too computationally demanding for screening approaches as intended here [44–46,56].

In a previous study, we established a computational protocol for predictive modeling based on DFT for binary III-V compounds over a wide range of strain values [45]. In this study, we are now extending this approach to ternary III-V compounds, which then allow the combination of strain and composition to fully explore a band gap design approach. For ternary systems, only the effects of composition variations on the band gap in unstrained materials have been studied [40,41,44,51–55]. For strained materials, a suitable theoretical framework is still lacking. We present here a predictive first-principles protocol for a complete mapping of the mutual correlation of composition, strain, and band gap in ternary III-V semiconductor systems. The goal is to provide guidelines for assessing and identifying the most promising target materials for experimental investigations in the future.

We start by describing the computational methods in Sec. II. Next, we describe the protocol for determining the nature of the band gap from supercell calculations using GaAsP as an example in Sec. III. We further present the composition-strain-band gap correlation results for different ternary III-V semiconductors in Sec. IV. We start with GaAsP, an experimentally well-studied and promising candidate for LEDs, detectors, and Si-based multijunction solar cells [57–64]. The results for the GaAsN compound, a promising laser-active material [44,65–67], are presented next. To show the general applicability of our approach, we then show selected results for (i) GaPSb, a candidate for vertical cavity emitting surface laser [68–72]; (ii) GaAsSb, a material for tandem solar cell application [73,74]; (iii) GaPBi, a promising material for nearinfrared photonic device application on Si [75,76]; and (iv) GaAsBi, another material discussed for near and midinfrared photonic device application [77–79]. We then discuss the comparison of our computations with experimental data in Sec. V, underlining the accuracy and predictive capability of our computational approach.

II. COMPUTATIONAL DETAILS

The calculations were performed with DFT-based approaches as implemented in the Vienna *ab initio* simulation package (VASP 5.4.4) [80–83], using plane wave basis sets in conjunction with the projector-augmented wave (PAW)

approach [84,85]. The ternary materials were generated using the special quasirandom structures (SQS) approach [86] with a supercell of size $6 \times 6 \times 6$. The SQS cells were generated using the alloy theoretic automated toolkit (ATAT) [87–89]. For all the materials except GaAsN, one SQS cell was used per composition. In GaAsN, in agreement with the previous observation [44], we found that the size of the band gap strongly depends on the distribution of N atoms in the supercell, even in the SQS approach. We thus used 10 SQS cells for each composition in this case.

Geometry optimization of the supercells was performed using the PBE functional [90], including the dispersion-correction method DFT-D3 with an improved damping function [91,92]. The basis set energy cutoff was set to 450 eV. The electronic energy convergence criteria of 10^{-6} eV and the force convergence of 10^{-2} eVÅ^{-1} were used. The reciprocal space was sampled at the Γ point only, given the large supercells used [93]. The meta-GGA functional TB09 [47] was used to calculate the electronic properties (band gaps and band structures). The effects of spin-orbit coupling were considered in the TB09 calculations. For the meta-GGA calculations, the energy cutoff of the basis set and the convergence criterion for the electronic energy were lowered to 350 eV and 10^{-4} eV, respectively, to reduce the computational costs. Structure optimizations were carried out by consecutive volume and position optimization until convergence was reached. This setup was previously used to generate band gaps in excellent agreement with experimental data [44].

All the materials within the composition range investigated here feature the zincblende-type structure only. Moreover, [100] crystal direction is the most common choice of substrate orientation and growth direction in epitaxy. Therefore, we modeled the strain application along [100] directions only. The isotropic strain was modeled by increasing (decreasing) all the lattice parameters of the unstrained structure by the same amount. In this case, only the atomic positions of the strained structure were optimized, keeping the volume fixed. For biaxial strain, the in-plane lattice parameters were kept fixed, and the lattice parameter in the out-of-plane direction was optimized. No structural phase transition is assumed under strain application. More details on the strain modeling can be found in Ref. [45]. In the following, we indicate tensile strain with a positive sign and compressive strain with a negative sign.

DFT calculations were performed at discrete points in composition-strain space (Fig. S6 [94]). The calculated band gap values were then interpolated to create the final images in Figs. 2–6. Noticeably, for the systems we addressed in this article, the variations of band gap values with concentration and strain are mostly nonmonotonic (Fig. S6 [94]). This resulted in nonsmooth interpolation in Figs. 2–6. It is to be stressed that the origin of the nonsmooth patterns is neither an interpolation artifact nor a deficiency of our DFT protocol. This solely originated because of the nonmonotonic variation of the band gap values (in the composition-strain space) of the SQS cells that we used to calculate band gaps. A choice of positive smoothening during interpolation (e.g., bivariate B-spline, gaussian filtering) could mitigate the problem but significantly increased the deviation of the interpolated band gap values from the calculated DFT values and was thus not

chosen. Further detail of the interpolation procedures can be found in Sec. SVI [94]. Moreover, the nature of band gaps can solely be deduced from the direct-indirect transition lines and thus requires no interpolation.

III. PROTOCOL FOR DETERMINING BAND GAP NATURE

Supercell calculations, as required for modeling ternary semiconductors, lead to the folding of band structures [104,105]. The size of the band gap can be well extracted from the folded band structure, which represents the energy difference between the highest occupied VB and the lowest unoccupied CB obtained from supercell calculations (folded bands). However, determining the band gap's nature requires the primitive Bloch character of the bands to be known, which gets mixed up in the supercell eigenstates. With the band unfolding method, one projects these supercell eigenstates on the eigenstates of a suitable reference primitive cell. This requires the calculation of Bloch spectral weights (BSW), which measure the fraction of the primitive Bloch character in a supercell eigenstate. The result is an effective band structure (EBS) [51–55]. The spectral weights, $w_{n,\mathbf{K}}(\mathbf{k})$, can be calculated from the plane wave coefficients as described in Ref. [55]:

$$w_{n,\mathbf{K}}(\mathbf{k}_j) = \sum_{\mathbf{g}} |C_{n,\mathbf{K}}(\mathbf{g} + \mathbf{G}_j)|^2, \qquad (1)$$

where n represents the band index, and the reciprocal lattice vectors of the primitive and supercell are denoted by $\mathbf{g}$ and $\mathbf{G}_j$, respectively. The index j accounts for the series of primitive vectors, $\mathbf{k}_j = \mathbf{K} + \mathbf{G}_j$. The code "fold2Bloch" from Ref. [54] was used to calculate the BSW values.

In our previous study on binary III-V systems [45], we have shown that the valence band maxima (VBM) always remain at the Γ point, and only the conduction band minima (CBM) change their position in reciprocal space under strain. We have also shown that the CBM occurs only at the Γ, L, and (near) X point in the band structure under strain. Therefore, it is sufficient to trace the conduction band (CB) at these points to determine the nature of the band gap. As in our previous study on binary systems, we focus here on analyzing ternary III-V compounds with zincblende structures. For these structures in the $6 \times 6 \times 6$ supercell dimensions chosen here, the Γ, L, and X point of the primitive band structure fold to the Γ point in the supercell [53–55]. Therefore, it is sufficient to calculate the BSWs of solely the CB at the Γ point in the supercell calculation to determine the nature of the band gap. Consequently, we performed the supercell calculations by sampling the reciprocal space only at the Γ point and unfolded the CB.

Figure 1 shows the steps for determining the band gap nature from supercell calculations more clearly. Figure 1(a) shows the band gap variation for GaAsP with 3.7% P concentration under isotropic compressive strain. The Γ, L, and X BSWs of the folded supercell CB are given in parentheses. This shows 100% Γ BSW for the unstrained structure in line with the direct band gap. With increasing strain, the Γ BSW decreases (first number in brackets), and the L BSW increases (second number in brackets). After a certain amount of strain, the L character of the CB dominates. The band gap
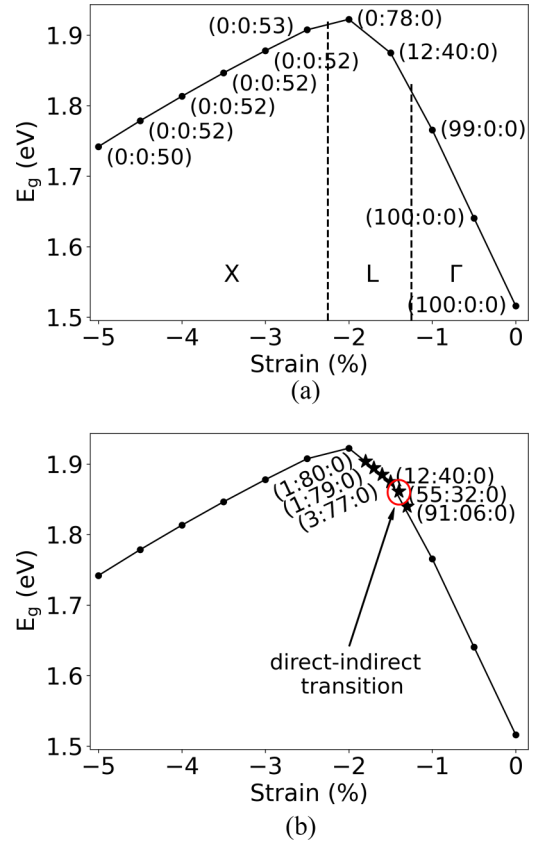

FIG. 1. Variation of the band gap under isotropic compressive strain for GaAs$_{0.963}$P$_{0.037}$. The Γ, L, and X BSW of the folded supercell conduction band are given in parentheses in the format (Γ:L:X). The vertical lines in (a) separate regions where the CBM changes character. In (b), the strain resolution is increased to determine the point of direct-indirect transition more accurately, indicated by the red circle (where the highest BSW changes from Γ to L).

becomes indirect in nature. Notably, once the strain values reach the point of direct-indirect transition (DIT) in the band gap nature (around -1.5% strain), the band gap values begin to decrease further with additional strain. This trend is like what we previously observed in binary III-V semiconductor systems, where a strong dependence of the band energies (E) on the wavevectors ($\mathbf{k}$) under strain was found, leading to a nonmonotonic variation of band gap values with strain [45]. Moreover, we found that such nonmonotonic behavior in band gap values under strain points to a DIT [45]. In ternary III-V semiconductor systems, we have now found that similar nonmonotonic behavior in band gap values under strain also indicates a DIT. Further compressing the system then leads to a transition of the CB character from L to X.

In Fig. 1(b), we show calculations with increased resolution in strain to accurately determine the transition to L corresponding to the sought point of DIT at -1.4% strain. We define the last strained structure with band gap of direct nature before the transition to the indirect band gap as the transition point [the red circle in Fig. 1(b)]. In the Supplemental Material (Fig. S1 [94]), we have given the EBSs of GaAs$_{0.963}$P$_{0.037}$ for different strain values. These confirm our analyses.

If the difference in BSW between different points in k-space is large, the nature of the band gap can be unanimously determined. However, close to the transition points, in some cases, the differences are more subtle (Fig. S2 [94]). We, therefore, set a cutoff criterion of 20% BSW. If the Γ BSW is larger than the cutoff criterion, then the direct transition has a finite probability even if the L or X BSW is larger than the Γ BSW. In such cases, the band gap is called "partially direct." This defines a "region of uncertainty" in the band gap nature. We chose the 20% cutoff criterion because this produces results that agree best when compared to the experiments for several systems. For the GaPBi system, however, the 10% BSW cutoff criterion produces the best agreement.

In some systems such as GaAsN, the band originating from the added nitrogen atoms, the so-called "defect N state" [54,106–109], is strongly dispersed under strain (Figs. S3b and S4b [94]). Therefore, we set another cutoff criterion of 20% BSW as a minimum limit for a (defect) eigenstate to be considered an eigenstate (Fig. S5 [94]). Starting from the lowest unoccupied CB, we search for eigenstates until the cutoff BSW criterion is met, at which point we consider it to be the redefined CB. If none of the CBs satisfy the cutoff criterion, we use the lowest CB for determining the band gap nature. Accordingly, in these cases, we calculate the band gap values as the energy difference between the highest VB and the redefined CB. When redefining, unoccupied CB states that do not satisfy the cutoff criteria are disregarded. This led to an increase in the band gap values, as is observed in Fig. S5 [94].

IV. RESULTS

In this section, we present the band gaps calculated for different materials and determine their nature according to the above protocol. We mapped the band gaps in terms of their size and nature for various strained ternary III-V compounds. We start with two important ternary III-V semiconductor materials, GaAsP and GaAsN. Then we show selected data for the material systems GaPSb, GaAsSb, GaPBi, and GaAsBi.

A. GaAsP

For the case of isotropic strain, Fig. 2 shows the band gap as a function of composition ($x = 0$–100% in GaAs$_{1-x}$P$_x$) from 5% tensile to 5% compressive strain. The band gap value varies between 0.32 and 2.42 eV in the strain regime investigated. For the same amount of P concentration, the band gap primarily increases in moving from tensile to compressive. Furthermore, the figure shows that in going from compressive to tensile strain, the DIT occurs at a higher concentration of P atoms. The dashed horizontal line marks the data corresponding to the unstrained structures for different fractions of P. The intersection of this line with the DIT line shows at which percentage of phosphorous contribution the unstrained structure shows a DIT. This transition occurs at $x = 37\%$. Here, the band gap shows a value of 1.96 eV. The terms direct and indirect in the figure correspond to the area where the band gap is direct and indirect, respectively. Due to the similarity with commonly used phase diagrams, we call this representation a "band gap phase diagram." This and the
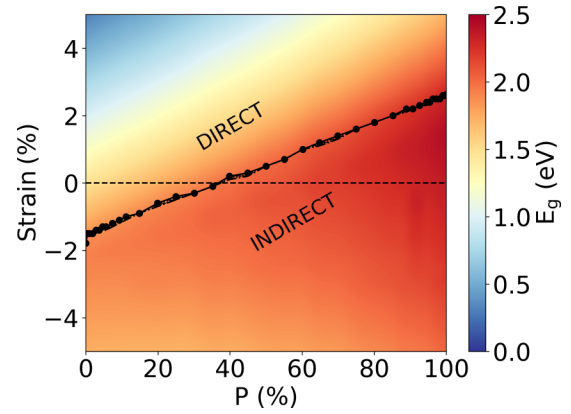

FIG. 2. Isotropic strain for GaAsP. The variation of band gap magnitudes (E_g) and type as a function of composition and strain. The dashed black horizontal line indicates unstrained GaAsP. The black circles are the calculated DIT points. The direct and indirect enclosed regions describe the nature of band gap being direct and indirect, respectively. The hatched pattern region is the "uncertainty region" (see Sec. III).

following figures thus provide a 2D representation of the band gap phase diagram for the ternary materials.

For the biaxial strain regime, Fig. 3 shows the band gap phase diagram for GaAsP as a function of composition from 5% tensile to 5% compressive strain. The value of the band gap varies in a range of 0.82–2.42 eV. For the same amount of P atoms, the band gap reaches a maximum around the unstrained structure and gets smaller for tensile as well as compressive strain. This is different from the isotropic strain case. For unstrained GaP, the band gap value is 2.36 eV. The nature of the band gap also shows a different trend compared to Fig. 2. The range of strain around the unstrained structure where a direct band gap is found gets smaller for higher
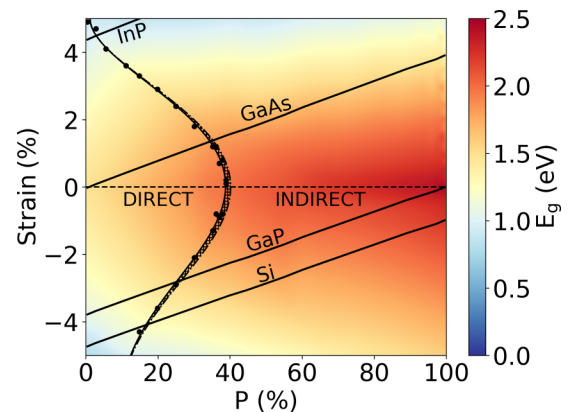

FIG. 3. Biaxial strain for GaAsP. The variation of band gap magnitudes (E_g) and type as a function of composition and strain. The dashed black horizontal line indicates unstrained GaAsP. The black circles are the calculated DIT points. The DIT points are fitted with a fifth-order polynomial. The direct and indirect enclosed regions describe the nature of band gap being direct and indirect, respectively. The hatched pattern region is the "uncertainty region" (see Sec. III). Solid black lines indicate the substrate lines under "epitaxial growth" model.

amounts of P. This is in line with GaAs (0% P) being a direct and GaP (100% P) being an indirect semiconductor. The largest amount of P concentration where a direct semiconductor is found is 39–40% P in the unstrained structure. This is similar to the previous experimental result (45% P) [10,110].

One of the most common approaches to experimentally realize biaxial strain in III-V semiconductors is epitaxial growth. As pointed out in Ref. [45], biaxial strain can be used to model epitaxial growth. We thus investigate the effect of different substrates in our band gap phase diagram (Fig. 3), where each solid line corresponds to one substrate: GaAs, GaP, InP, or Si. These solid lines indicate how much biaxial strain would develop in the GaAsP system as the respective value of % P when grown on the respective substrates under idealized conditions. The (substrate) strains are calculated according to Eq. (2):

$$\text{Substrate strain}(\%) = \frac{a_{\text{sub}} - a}{a} \times 100, \qquad (2)$$

where a_{sub} is the equilibrium lattice parameters of the substrates, and a is the lattice parameters of unstrained GaAsP systems at their respective P concentrations, e.g., for 100% P, the strain on the GaP substrate is zero, while growing GaAs (0% P) on GaP would result in 3.8% in-plane compressive strain. This, of course, neglects defect formation and strain relaxations and assumes perfect epitaxial growth. Clearly, by choosing different substrates, the nature can be changed, and the size of the band gap can be tuned over a wide range. We refer to the next section for a comparison of our calculations to experimental data.

B. GaAsN

As the next material, we investigate GaAsN. First, we show results for isotropic strain, which results in the band gap phase diagram shown in Fig. 4. The results are markedly different from GaAsP, and the data set is much more limited. In this case, we found a strong dependency of the band gap on the N atoms distribution in the supercell [44]. We thus used 10 SQS cells for each data point in the figure and averaged the resulting band gaps. This results in an error bar for the DIT points, which is rather large for medium amounts of nitrogen atoms due to the formation of small clusters and chains. Calculations were only possible for up to 12% N. For higher concentration and/or high compressive strain, our chosen supercell is not large enough to avoid the unphysical electronic interaction of N atoms with their images in the periodic boundary condition approach. This effect has already been discussed in Ref. [44]. For the strain and composition regions where computation was possible, an indirect gap is only found for low values of % N and rather large compressive strain values. The EBSs for selected % N and strain values are shown in Figs. S3 and S4 [94].

For biaxial strain in GaAsN, the data are shown in Fig. 5. In contrast to GaAsP, the band gap gets smaller with the increasing amount of nitrogen in the system, from 1.47 eV for the unstrained case of GaAs to 0.10 eV for the highly strained systems with a large number of N atoms. All band gaps computed are direct. Epitaxial growth on GaAs is reasonably
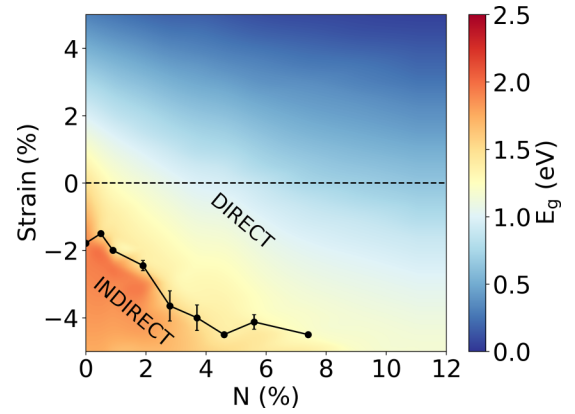

FIG. 4. Isotropic strain for GaAsN (up to 12% N). The variation of band gap magnitudes (E_g) and type as a function of composition and strain. The dashed black horizontal line indicates unstrained GaAsN. The black circles are the calculated DIT points. Beyond 7% N, the DIT is outside the investigated strain regime. 10 SQS cells are used for each configuration and strain point. The band gaps plotted are the average band gaps. The error bars indicate the standard deviation in DIT points estimation. The direct and indirect enclosed regions describe the nature of band gap being direct and indirect, respectively.

possible for moderate strain values and results in a variation of band gap from 1.47 eV to 0.45 eV. For GaP and Si substrates, a large strain would be exerted on the system, and mostly lower band gap values are found.

C. GaPSb, GaAsSb, GaPBi, GaAsBi

The approach outlined here can be extended to other combinations of elements in III-V semiconductor materials. Exemplarily, we present the band gap phase diagrams for four other important ternary compounds in Fig. 6. Since epitaxial growth is the most interesting experimental realization method for these compounds, we only present the data for biaxial strain.
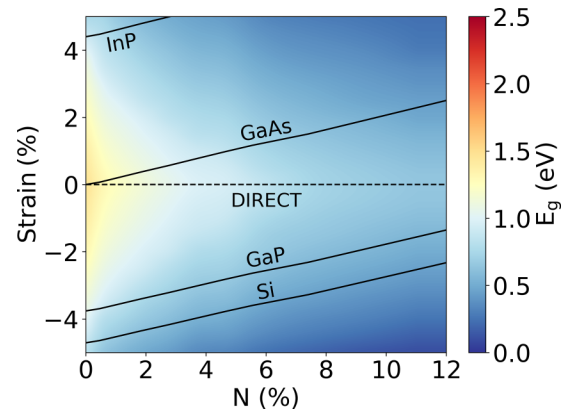

FIG. 5. Biaxial strain for GaAsN (up to 12% N). The variation of band gap magnitudes (E_g) and type as a function of composition and strain. The dashed black horizontal line indicates unstrained GaAsN. 10 SQS cells are used for each configuration and strain point. The band gaps plotted are the average band gaps. All the band gaps are direct in nature. Solid black lines indicate the substrate lines under the "epitaxial growth" model.
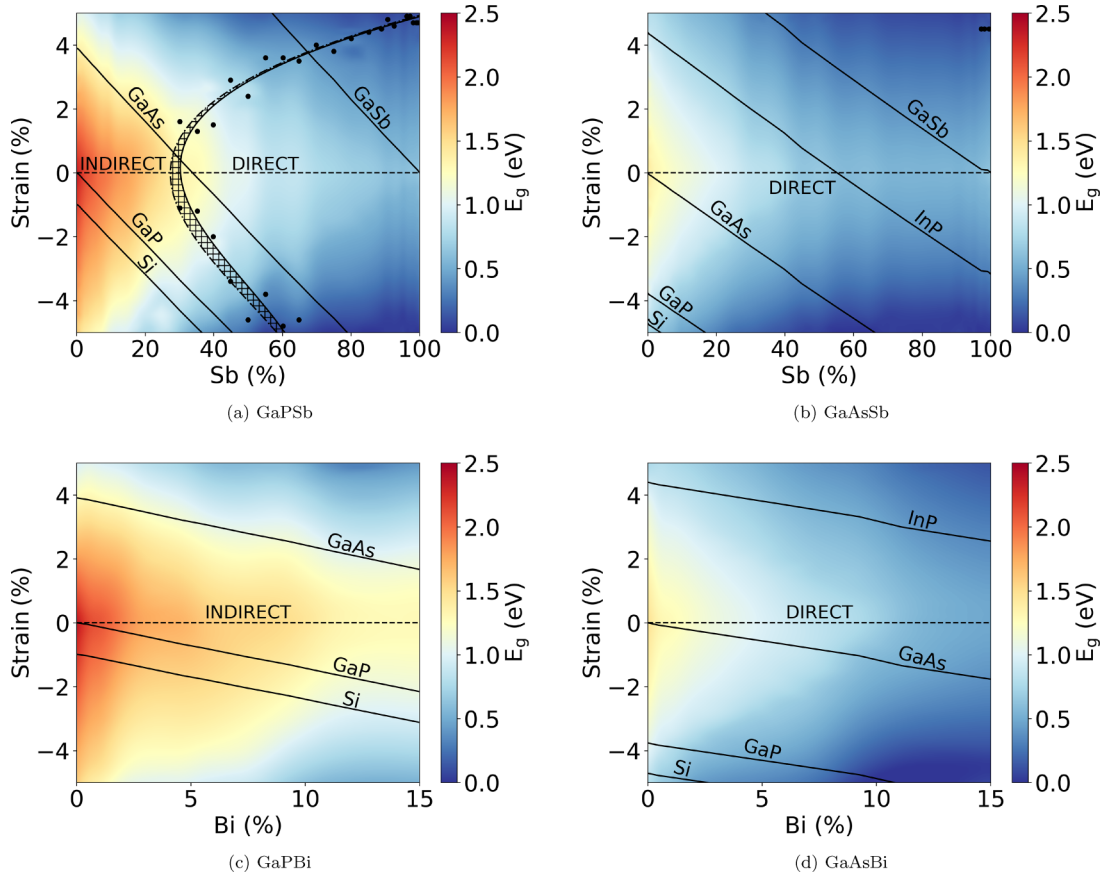
FIG. 6. Band gap phase diagram for ternary III-V semiconductors GaEY (E = P, As; Y = Sb, Bi) under biaxial strain. The band gap magnitudes (E_g) are shown in the color bar. The dashed black horizontal line indicates unstrained structures. The black circles are the calculated DIT points. The direct and indirect enclosed regions describe the nature of band gap being direct and indirect, respectively. The hatched pattern region is the "uncertainty region" (see Sec. III). Solid black lines indicate the substrate lines under the "epitaxial growth" model.

For all compounds investigated, we find a band gap range of 0.00–2.36 eV, with the largest values found for the host materials GaP and GaAs in the unstrained case. The alloys with Sb could be investigated over the full range of 0–100% Sb in GaPSb and GaAsSb [Figs. 6(a) and 6(b)]. We find a DIT for unstrained GaPSb at 30% Sb concentration [Fig. 6(a)]. For this compound, the DIT is shown as a region, including the uncertainty in determining the nature of the band gap, as outlined in Sec. III. With the increase in the Sb fraction, the strain at which the DITs take place increases. For GaAsSb and GaAsBi, the band gap is direct throughout the range investigated [Figs. 6(b) and 6(d)], while it is indirect for GaPBi [Fig. 6(c)]. Notably, we only investigate the bismides up to a fraction of 15% Bi. The reason is that, similar to GaAsN (Fig. S4 [94]), for structures with large Bi content, the strongly dispersed bands decrease the reliability in the determination of band gap nature. Additionally, GaPBi and GaAsBi become metallic for higher Bi fractions. Although we find no transition within 15% Bi, it can not be excluded that the DIT appears at higher percentages of bismuth.

Again, we indicate the strain values associated with different typical substrates for epitaxial growth by solid black lines in the figures. The data show that deviating from the substrate-layer lattice-matching condition quickly leads to high strain,

and defects are highly likely to occur during growth. Also, Si can be used as a substrate for GaPSb and GaPBi epitaxial growth if the Sb or Bi content is not too large. The epitaxial growth of the respective GaAs-based materials (GaAsP, GaAsN, GaAsSb, GaAsBi) will give rise to high strain on Si substrate throughout the whole composition region. A noticeable change in the slope in substrate lines is found close to 10% Bi and 40% Sb concentration in GaAsBi and GaAsSb, respectively. Although we did not find any structural phase transition in those regions, the origin of the change in the slope is not clear to us yet.

From the above discussions, it becomes clear that band gap phase diagrams can be a valuable aid in deciding which substrates are good choices for targeting a specific band gap size and nature for a given ternary material. And vice versa, which material to grow for a specific application and a given substrate? We will discuss this further in the next section.

V. DISCUSSION

All data were derived from DFT computations to this point. In Table I, we now compare our calculated band gaps with experimental data from measurements on heteroepitaxial layer structures. The GaAsP/GaAs samples were grown

TABLE I. Comparison of the calculated band gaps for investigated ternary III-V semiconductors under biaxial strain with experiments. The experimental data are for the heteroepitaxial layer structures, and the band gaps are determined from photoluminescence (PL) measurements. The "I" in the brackets indicate the indirect nature of the band gap. The remaining band gaps are direct. (RT-PL: room temperature PL)

System	Substrate	x(%)	Layer Thickness (nm)	Band gap (eV) Calculated	Band gap (eV) Experiment	Deviation (eV)	Percentage Deviation (%)	RMSD[a] (eV)
GaAs$_{1-x}$P$_x$ [111]	GaAs	18.0	9000	1.65	1.66	0.01	0.6	0.01
		25.0	12250	1.72	1.72	0.00	0.0	
		28.0	13000	1.75	1.76	0.01	0.6	
GaP$_{1-x}$Sb$_x$[b] [72]	GaP	14.0	–	1.66(I)	1.61(I)	−0.05	−3.1	0.10
	GaAs	29.0	–	1.33(I)	1.39(I)	0.06	4.3	
		32.0	–	1.30	1.31	0.01	0.8	
		37.0	–	1.24	1.33	0.09	6.8	
	GaSb	93.0	–	0.56	0.74	0.18	24.3	
GaAs$_{1-x}$Sb$_x$	GaAs	5.5	46.3	1.22	1.34	0.12	9.0	0.13
		7.0	51.2	1.17	1.31	0.14	10.7	
GaAs$_{1-x}$Bi$_x$ [112,113,115] [116–118]	GaAs	0.9	75.0	1.28	1.33	0.05	3.8	0.10
		1.9	67.0	1.19	1.26	0.07	5.6	
		2.9	60.0	1.10	1.20	0.10	8.3	
		3.2	59.0	1.08	1.18	0.10	8.5	
		3.8	54.0	1.04	1.14	0.10	8.8	
		4.8	25.0	0.98	1.11	0.13	11.7	
		5.3	50.0	0.95	1.07	0.12	11.2	
		6.0	25.0	0.91	1.04	0.13	12.5	
GaAs$_{1-x}$N$_x$ [10,44,114]	GaAs	1.2	6.3	1.20	1.25	0.05	4.0	0.12
		2.0	17.0	1.10	1.16	0.06	5.2	
		2.3	7.0	1.06	1.17	0.11	9.4	
		2.9	7.0	1.00	1.11	0.11	9.9	
		5.0	4.0	0.82	1.01	0.19	18.8	
GaAs$_{1-x}$Sb$_x$	GaAs	27.8	3.7	0.67	1.10	0.43	39.1	0.42
		28.0	4.1	0.66	1.07	0.41	38.3	
GaAs$_{1-x}$N$_x$ [10,44,114]	GaP	4.9	6.0	0.66	1.18	0.52	44.1	0.66
	Si	6.9	5.5	0.47	1.21	0.74	61.2	
		8.9	5.5	0.46	1.17	0.71	60.7	
		9.5	6.0	0.45	1.11	0.66	59.5	
		10.9	5.4	0.45	1.11	0.66	59.5	
GaP$_{1-x}$Sb$_x$	Si	⩽17.5	7–9	1.91–1.36(I)	No RT-PL observed			
GaP$_{1-x}$Bi$_x$ [112]	GaP	⩽12.0	17–73	2.03–1.18(I)	No RT-PL observed			

[a]Calculated from all samples per system.

[b]For GaPSb samples, no specific thicknesses were reported in the reference.

by low-pressure hydride vapor phase epitaxy (LP-HVPE). Further details can be found in Ref. [111]. The remaining samples were grown by metalorganic vapor phase epitaxy (MOVPE). The details of the growth characteristics of the MOVPE samples can be found in Refs. [22,72,112–117]. Experimentally, the layer thickness and band gaps of the MOVPE samples were determined using x-ray diffraction and room-temperature photoluminescence (RT-PL), respectively. Except for GaPSb samples from Ref. [72], in which cases, the PL were measured at 10 K.

The comparison of the experimental band gaps with our computed results shows good agreement. The deviation is determined with respect to the root-mean-square deviation (RMSD) from all available experimental samples. For most structures, the RMSD is around 0.1 eV. Most computed values deviate by less than 10% from the experimental values (exceptions are discussed separately); in the case of GaAsP, the deviation is even more accurate (< 1%). This confirms our previous findings on unstrained structures that the DFT protocol we developed gives excellent agreement to experimental band gaps [11,40,44,45]. In this study, we show that it is also applicable to compound semiconductors under strain. For samples with very small layer thickness, the matching of experiment and computation is less good. This can be observed

for GaAsSb/GaAs thin samples with RMSD of ca. 0.4 eV. We attribute this to the 2D quantum confinement effect, which is found for thin samples. This confinement effect leads to an increase in the band gap with respect to thicker samples [119]. This effect is not captured in our computational model as the calculations were performed for 3D periodic strained structures. The large deviation observed for GaAsN/GaP and GaAsN/Si samples can not be explained by this effect alone, though. An additional effect here is the strong dependency of the band gap on the distribution of N atoms which has been found for unstrained GaAsN before [44]. The dependency is further amplified under large strain (around 3%, see Fig. 5) in those samples. In the case of GaAsN/GaAs samples, where the N concentration investigated was around 1–5%, the strain is relatively small ($< 1\%$), resulting in better agreement with the experiment as compared to the GaAsN/GaP and GaAsN/Si samples. No RT-PL was observed for GaPSb/Si and GaPBi/GaP samples. This is consistent with our findings that those materials show indirect band gaps [Figs. 6(a) and 6(c)]. Experimental measurements of the magnitude of the indirect band gaps are not available yet.

The consistent agreement between the experiment and calculated band gaps (both in magnitude and in nature) suggests that we are able to quantitatively predict the band gap over a wide range of compounds, compositions, and strain regions. However, as discussed above, the effect of 2D confinement is also crucial for relatively thin quantum well heterostructures and, hence, needs further investigation.

Finally, based on the band gap phase diagram, we propose several design strategies to optimize the selection of material combinations for achieving specific optical applications and new design principles for devices (Fig. 7).

In Fig. 7(a), we propose a quantum-well heterostructure (QWH) composed of biaxially strained GaAsP on GaAs substrate. As the QW layers are made out of a single material with varied composition only, the epitaxial growth could be performed efficiently. The band gap phase diagram shows the areas in compositional phase space where a direct band gap in $GaAs_{1-x}P_x$ can be achieved ($x < 34\%$). For $x > 35\%$, the band gaps are indirect and hence, are inappropriate for the heterostructure.

Figure 7(b) shows an efficient approach for the monolithic integration of multiple QWH to construct multijunction photovoltaics. In this case, the QWHs are separated by thin indirect band gap layers of the same material as QWH but only with a different composition. This would make the integration approach efficient, as no sample transfer is required during growth.

In Fig. 7(c), we propose a device with a gradual change in the band gap properties. The concept utilizes the continuous transition in the nature of band gap with alloy concentration in the vicinity of the DIT region. At the amount of P chosen here ($x = 15$–35%), we propose to grow the GaAsP epitaxial layer on GaP with P concentration continuously changing from the direct to indirect band gap region or vice versa. This way, changes in the band gap magnitude, as well as the nature of the band gap, are possible. Note that the concentration gradient can be implemented both in the horizontal and vertical directions.
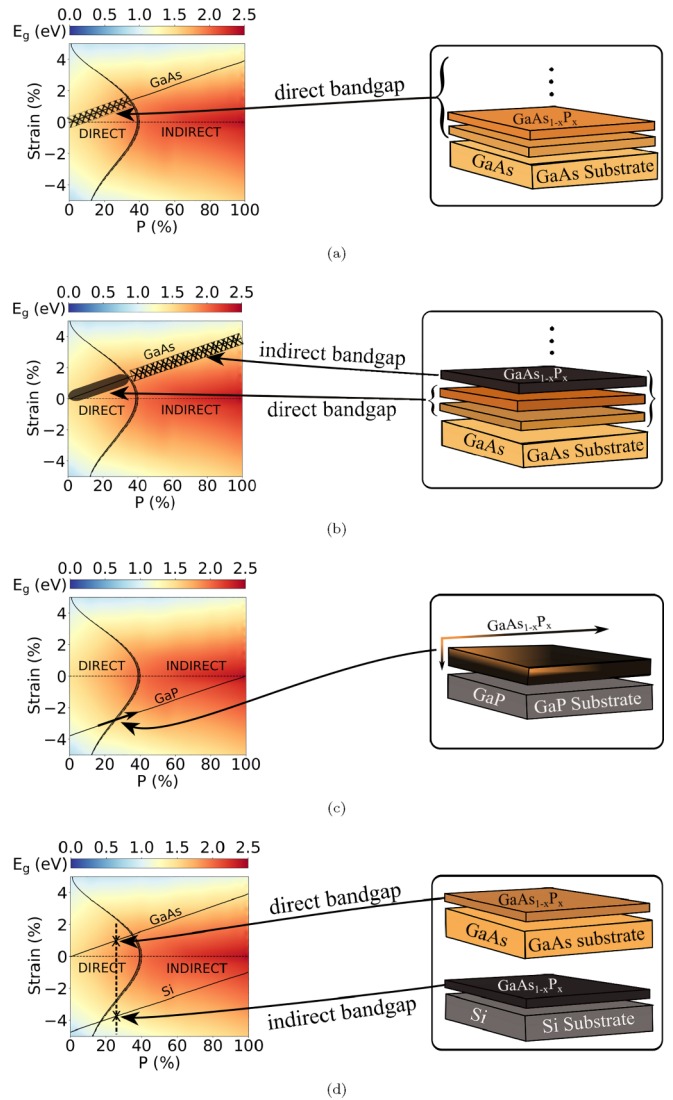

FIG. 7. Proposals on how the band gap phase diagram of biaxially strained GaAsP can be used in designing optoelectronic devices. (a) Defines the bound of composition region for creating a QWH with direct band gap GaAsP on GaAs substrate. (b) Choosing the different composition regions appropriately to make a multijunction photovoltaic with successive direct and indirect cells on the GaAs substrate. (c) In the vicinity of the transition point, the band gap properties of the GaAsP epilayer on the GaP substrate can be changed by appropriately varying the composition. (d) Depending on the choice of substrate, GaAs or Si, the particular composition indicated by the vertical line can be made direct or indirect band gap, respectively.

Figure 7(d) shows another application of this concept. By appropriately choosing the substrate, we can tune the epitaxial layer (here: GaAsP) to show either a direct or indirect band gap. Depending on the substrate, GaAs or Si, the particular composition indicated by the vertical line will show direct or indirect band gap, respectively.

VI. SUMMARY

Using density functional theory and the concept of band unfolding, we developed a first-principles computational protocol for the comprehensive mapping of the band gap magni-

tude and type over a wide range of composition and strain values for several ternary III-V semiconductors. We constructed the composition-strain-band gap relationship, the band gap phase diagram, for several ternary III-V semiconductors: GaAsP, GaAsN, GaPSb, GaAsSb, GaPBi, and GaAsBi. We showed that this way of mapping the effect of strain could be used to choose application-specific best-suited material systems and hence, is highly beneficial to device design. In addition, we developed an efficient approach based on Bloch spectral density for determining the nature of band gap from supercell calculation. Notably, our computational protocol can be generalized to explore the vast chemical space of III-V materials with all other possible combinations of III and V elements. The comparison to experimental band gap data underlines the accuracy of the computational approach chosen. This approach will be extended to more complex materials in the future.

The density functional theory calculations data are openly available in the NOMAD repository [120]. The interactive band gap phase diagrams (in HTML format) are available in the Supplemental Material [94]. To view the diagrams, open the HTML files in a web browser. Alternatively, the diagrams can be viewed directly on GitHub [121], last accessed 10.05.2023).

[1] R. Soref, Proc. IEEE **81**, 1687 (1993).

[2] P. Y. Yu and M. Cardona, *Fundamentals of Semiconductors: Physics and Materials Properties*, Graduate Texts in Physics (Springer Berlin Heidelberg, 2010).

[3] T. Hepp, J. Lehr, R. Günkel, O. Maßmeyer, J. Glowatzki, A. Ruiz Perez, S. Reinhard, W. Stolz, and K. Volz, Electron. Lett. **58**, 70 (2022).

[4] C. Fuchs, A. Brüggemann, M. J. Weseloh, C. Berger, C. Möller, S. Reinhard, J. Hader, J. V. Moloney, A. Bäumner, S. W. Koch, and W. Stolz, Sci. Rep. **8**, 1422 (2018).

[5] S. Mokkapati and C. Jagadish, Mater. Today **12**, 22 (2009).

[6] F. Dimroth, T. N. D. Tibbits, M. Niemeyer, F. Predan, P. Beutel, C. Karcher, E. Oliva, G. Siefer, D. Lackner, P. Fuß-Kailuweit, A. W. Bett, R. Krause, C. Drazek, E. Guiot, J. Wasselin, A. Tauzin, and T. Signamarcheix, IEEE J. Photovolt. **6**, 343 (2016).

[7] B. Mitchell, G. Peharz, G. Siefer, M. Peters, T. Gandy, J. C. Goldschmidt, J. Benick, S. W. Glunz, A. W. Bett, and F. Dimroth, Prog. Photovolt: Res. Appl. **19**, 61 (2011).

[8] S. P. Philipps, F. Dimroth, and A. W. Bett, in *McEvoy's Handbook of Photovoltaics*, edited by S. A. Kalogirou (Elsevier, 2018), 3rd Ed., pp. 439–472.

[9] A. Beyer, W. Stolz, and K. Volz, Prog. Cryst. Growth Charact. Mater. **61**, 46 (2015).

[10] I. Vurgaftman, J. R. Meyer, and L. R. Ram-Mohan, J. Appl. Phys. **89**, 5815 (2001).

[11] A. Beyer, N. Knaub, P. Rosenow, K. Jandieri, P. Ludewig, L. Bannow, S. W. Koch, R. Tonner, and K. Volz, Appl. Mater. Today **6**, 22 (2017).

[12] P. Ludewig, S. Reinhard, K. Jandieri, T. Wegele, A. Beyer, L. Tapfer, K. Volz, and W. Stolz, J. Cryst. Growth **438**, 63 (2016).

[13] S. Liebich, M. Zimprich, A. Beyer, C. Lange, D. J. Franzbach, S. Chatterjee, N. Hossain, S. J. Sweeney, K. Volz, B. Kunert, and W. Stolz, Appl. Phys. Lett. **99**, 071109 (2011).

[14] O. Supplie, O. Romanyuk, C. Koppka, M. Steidl, A. Nägelein, A. Paszuk, L. Winterfeld, A. Dobrich, P. Kleinschmidt, E. Runge, and T. Hannappel, Prog. Cryst. Growth Charact. Mater. **64**, 103 (2018).

[15] G. Stringfellow, in *Metalorganic Vapor Phase Epitaxy (MOVPE): Growth, Materials Properties, and Applications* (Wiley, 2019), pp. 19–69.

[16] K. Volz, J. Koch, F. Höhnsdorf, B. Kunert, and W. Stolz, J. Cryst. Growth **311**, 2418 (2009).

[17] M. Feifel, J. Ohlmann, J. Benick, T. Rachow, S. Janz, M. Hermle, F. Dimroth, J. Belz, A. Beyer, K. Volz, and D. Lackner, IEEE J. Photovolt. **7**, 502 (2017).

[18] B. Kunert, J. Koch, T. Torunski, K. Volz, and W. Stolz, J. Cryst. Growth **272**, 753 (2004).

[19] K. Volz, T. Torunski, B. Kunert, O. Rubel, S. Nau, S. Reinhard, and W. Stolz, J. Cryst. Growth **272**, 739 (2004).

[20] J. Veletas, T. Hepp, K. Volz, and S. Chatterjee, J. Appl. Phys. **126**, 135705 (2019).

[21] T. Wegele, A. Beyer, P. Ludewig, P. Rosenow, L. Duschek, K. Jandieri, R. Tonner, W. Stolz, and K. Volz, J. Phys. D: Appl. Phys. **49**, 075108 (2016).

[22] T. Hepp, L. Nattermann, and K. Volz, in *Bismuth-Containing Alloys and Nanostructures*, edited by S. Wang and P. Lu, Springer Series in Materials Science, Vol. 285 (Springer, Singapore, 2019), pp. 37–58.

[23] P. E. Van Camp, V. E. Van Doren, and J. T. Devreese, Phys. Rev. B **41**, 1598 (1990).

[24] R. F. Potter, Phys. Rev. **103**, 861 (1956).

[25] P. A. Alekseev, V. A. Sharov, B. R. Borodin, M. S. Dunaevskiy, R. R. Reznik, and G. E. Cirlin, Micromachines **11**, 581 (2020).

[26] A. K. Katiyar, K. Y. Thai, W. S. Yun, J. Lee, and J.-H. Ahn, Sci. Adv. **6**, eabb0576 (2020).

[27] B. Lim, X. Y. Cui, and S. P. Ringer, Phys. Chem. Chem. Phys. **23**, 5407 (2021).

[28] G. Signorello, E. Lörtscher, P. Khomyakov, S. Karg, D. Dheeraj, B. Gotsmann, H. Weman, and H. Riel, Nat. Commun. **5**, 3655 (2014).

[29] G. Signorello, S. Karg, M. T. Björk, B. Gotsmann, and H. Riel, Nano Lett. **13**, 917 (2013).

[30] L. Balaghi, G. Bussone, R. Grifone, R. Hübner, J. Grenzer, M. Ghorbani-Asl, A. V. Krasheninnikov, H. Schneider, M. Helm, and E. Dimakis, Nat. Commun. **10**, 2793 (2019).

[31] J. Grönqvist, N. Søndergaard, F. Boxberg, T. Guhr, S. Åberg, and H. Q. Xu, J. Appl. Phys. **106**, 053508 (2009).

[32] M. Hetzl, M. Kraut, J. Winnerl, L. Francaviglia, M. Döblinger, S. Matich, A. FontcubertaMorral, and M. Stutzmann, Nano Lett. **16**, 7098 (2016).

[33] M. Montazeri, M. Fickenscher, L. M. Smith, H. E. Jackson, J. Yarrison-Rice, J. H. Kang, Q. Gao, H. Hoe Tan, C. Jagadish, Y. Guo, J. Zou, M. E. Pistol, and C. E. Pryor, Nano Lett. **10**, 880 (2010).

[34] N. Sköld, L. S. Karlsson, M. W. Larsson, M.-E. Pistol, W. Seifert, J. Trägårdh, and L. Samuelson, Nano Lett. **5**, 1943 (2005).

[35] G. Bir and G. Pikus, *Symmetry and Strain-induced Effects in Semiconductors*, A Halsted Press book (Wiley, 1974).

[36] Y. Sun, S. E. Thompson, and T. Nishida, J. Appl. Phys. **101**, 104503 (2007).

[37] L. Tao, W. Ou, Y. Li, H. Liao, J. Zhang, F. Gan, and X. Ou, Semicond. Sci. Technol. **35**, 103002 (2020).

[38] G. Tsutsui, S. Mochizuki, N. Loubet, S. W. Bedell, and D. K. Sadana, AIP Adv. **9**, 030701 (2019).

[39] H. Fang, M. Madsen, C. Carraro, K. Takei, H. S. Kim, E. Plis, S. Y. Chen, S. Krishna, Y. L. Chueh, R. Maboudian, and A. Javey, Appl. Phys. Lett. **98**, 012111 (2011).

[40] L. C. Bannow, P. Rosenow, P. Springer, E. W. Fischer, J. Hader, J. V. Moloney, R. Tonner, and S. W. Koch, Modell. Simul. Mater. Sci. Eng. **25**, 065001 (2017).

[41] N. G. Anderson and S. D. Jones, J. Appl. Phys. **70**, 4342 (1991).

[42] Y. Tan, M. Povolotskyi, T. Kubis, T. B. Boykin, and G. Klimeck, Phys. Rev. B **94**, 045311 (2016).

[43] J. M. Jancu, R. Scholz, F. Beltram, and F. Bassani, Phys. Rev. B **57**, 6493 (1998).

[44] P. Rosenow, L. C. Bannow, E. W. Fischer, W. Stolz, K. Volz, S. W. Koch, and R. Tonner, Phys. Rev. B **97**, 075201 (2018).

[45] B. Mondal and R. Tonner-Zech, Phys. Scr. **98**, 065924 (2023).

[46] Y.-S. Kim, M. Marsman, G. Kresse, F. Tran, and P. Blaha, Phys. Rev. B **82**, 205212 (2010).

[47] F. Tran and P. Blaha, Phys. Rev. Lett. **102**, 226401 (2009).

[48] H. Jiang, J. Chem. Phys. **138**, 134115 (2013).

[49] G. Rehman, M. Shafiq, Saifullah, R. Ahmad, S. Jalali-Asadabadi, M. Maqbool, I. Khan, H. Rahnamaye-Aliabad, and I. Ahmad, J. Electron. Mater. **45**, 3314 (2016).

[50] D. Koller, F. Tran, and P. Blaha, Phys. Rev. B **85**, 155109 (2012).

[51] L. W. Wang, L. Bellaiche, S. H. Wei, and A. Zunger, Phys. Rev. Lett. **80**, 4725 (1998).

[52] P. V. C. Medeiros, S. S. Tsirkin, S. Stafström, and J. Björk, Phys. Rev. B **91**, 041116(R) (2015).

[53] V. Popescu and A. Zunger, Phys. Rev. Lett. **104**, 236403 (2010).

[54] O. Rubel, A. Bokhanchuk, S. J. Ahmed, and E. Assmann, Phys. Rev. B **90**, 115202 (2014).

[55] V. Popescu and A. Zunger, Phys. Rev. B **85**, 085201 (2012).

[56] Y. Hinuma, A. Grüneis, G. Kresse, and F. Oba, Phys. Rev. B **90**, 155405 (2014).

[57] M. G. Craford, D. L. Keune, W. O. Groves, and A. H. Herzog, J. Electron. Mater. **2**, 137 (1973).

[58] I. D. Henning and H. Thomas, Phys. Status Solidi A **79**, 567 (1983).

[59] Y. Tanaka and T. Toyama, IEEE Trans. Electron Devices **41**, 1475 (1994).

[60] T. Sato and M. Imai, Jpn. J. Appl. Phys. **41**, 5995 (2002).

[61] J. F. Geisz and D. J. Friedman, Semicond. Sci. Technol. **17**, 769 (2002).

[62] J. R. Lang, J. Faucher, S. Tomasulo, K. Nay Yaung, and M. Larry Lee, Appl. Phys. Lett. **103**, 092102 (2013).

[63] K. Hayashi, T. Soga, H. Nishikawa, T. Jimbo, and M. Umeno, Conf. Rec. IEEE Photovoltaic Spec. Conf. **2**, 1890 (1994).

[64] T. J. Grassman, D. J. Chmielewski, S. D. Carnevale, J. A. Carlin, and S. A. Ringel, IEEE J. Photovolt. **6**, 326 (2016).

[65] M. Weyers, M. S. Michio Sato, and H. A. Hiroaki Ando, Jpn. J. Appl. Phys. **31**, L853 (1992).

[66] B. Kunert, K. Volz, J. Koch, and W. Stolz, Appl. Phys. Lett. **88**, 182108 (2006).

[67] Y. Zhao, G. Chen, S. Wang, and S. F. Yoon, Thin Solid Films **450**, 352 (2004).

[68] S. Loualiche, A. Le Corre, S. Salaun, J. Caulet, B. Lambert, M. Gauneau, D. Lecrosnier, and B. Deveaud, Appl. Phys. Lett. **59**, 423 (1991).

[69] H. Shimomura, T. Anan, and S. Sugou, J. Cryst. Growth **162**, 121 (1996).

[70] K. Nakajima, T. Ujihara, S. Miyashita, and G. Sazaki, J. Cryst. Growth **209**, 637 (2000).

[71] H. B. Russell, A. N. Andriotis, M. Menon, J. B. Jasinski, A. Martinez-Garcia, and M. K. Sunkara, Sci. Rep. **6**, 20822 (2016).

[72] M. J. Jou, Y. T. Cherng, H. R. Jen, and G. B. Stringfellow, Appl. Phys. Lett. **52**, 549 (1988).

[73] M. J. Cherng, R. M. Cohen, and G. B. Stringfellow, J. Electron. Mater. **13**, 799 (1984).

[74] H. R. Jen, M. J. Cherng, and G. B. Stringfellow, Appl. Phys. Lett. **48**, 1603 (1986).

[75] T. M. Christian, D. A. Beaton, A. Mascarenhas, and K. Alberi, Proc. SPIE 10174, Int. Symp. Clust. Nanomater. **10174**, 101740F (2016).

[76] T. M. Christian, D. A. Beaton, K. Alberi, B. Fluegel, and A. Mascarenhas, Appl. Phys. Express **8**, 061202 (2015).

[77] S. J. Sweeney, Z. Batool, K. Hild, S. R. Jin, and T. J. C. Hosea, in *2011 13th International Conference on Transparent Optical Networks, Stockholm, Sweden* (IEEE, Piscataway, NJ, 2011), pp. 1–4.

[78] S. Wang, Y. Song, K. Wang, Y. Gu, H. Zhao, X. Chen, H. Ye, H. Zhou, C. Kang, Y. Li, C. Cao, L. Zhang, J. Shao, Q. Gong, and Y. Zhang, in *Asia Communications and Photonics Conference 2013* (OSA, Washington, D.C., 2013), p. AF3B.5.

[79] D. G. Cooke, F. A. Hegmann, E. C. Young, and T. Tiedje, Appl. Phys. Lett. **89**, 122103 (2006).

[80] G. Kresse and J. Hafner, Phys. Rev. B **47**, 558 (1993).

[81] G. Kresse and J. Hafner, Phys. Rev. B **49**, 14251 (1994).

[82] G. Kresse and J. Furthmüller, Phys. Rev. B **54**, 11169 (1996).

[83] G. Kresse and J. Furthmüller, Comput. Mater. Sci. **6**, 15 (1996).

[84] G. Kresse and D. Joubert, Phys. Rev. B **59**, 1758 (1999).

[85] P. E. Blöchl, Phys. Rev. B **50**, 17953 (1994).

[86] A. Zunger, S. H. Wei, L. G. Ferreira, and J. E. Bernard, Phys. Rev. Lett. **65**, 353 (1990).

[87] A. van de Walle, M. Asta, and G. Ceder, Calphad **26**, 539 (2002).

[88] A. van de Walle, Calphad **33**, 266 (2009).

[89] A. van de Walle, P. Tiwary, M. de Jong, D. Olmsted, M. Asta, A. Dick, D. Shin, Y. Wang, L.-Q. Chen, and Z.-K. Liu, Calphad **42**, 13 (2013).

[90] J. P. Perdew, K. Burke, and M. Ernzerhof, Phys. Rev. Lett. **77**, 3865 (1996).

[91] S. Grimme, J. Antony, S. Ehrlich, and H. Krieg, J. Chem. Phys. **132**, 154104 (2010).

[92] S. Grimme, S. Ehrlich, and L. Goerigk, J. Comput. Chem. **32**, 1456 (2011).

[93] H. J. Monkhorst and J. D. Pack, Phys. Rev. B **13**, 5188 (1976).

[94] See Supplemental Material at http://link.aps.org/supplemental/10.1103/PhysRevB.108.035202 for the effective band structures of GaAsP, GaAsN, and GaAsN under selected isotropic strain values; a visual representation of the assessment of uncertainty in the band gap nature near the direct-indirect transition region; the DFT calculated band gap values for all the systems described in the manuscript; the details of the interpolation procedure; and the band gap phase diagrams. The Supplemental Material also contains Refs. [45,52,95–103].

[95] P. V. C. Medeiros, S. Stafström, and J. Björk, Phys. Rev. B **89**, 041407(R) (2014).

[96] P. Virtanen, R. Gommers, T. E. Oliphant, M. Haberland, T. Reddy, D. Cournapeau, E. Burovski, P. Peterson, W. Weckesser, J. Bright, S. J. van der Walt, M. Brett, J. Wilson, K. J. Millman, N. Mayorov, A. R. J. Nelson, E. Jones, R. Kern, E. Larson, C. J. Carey *et al.*, Nat. Methods **17**, 261 (2020).

[97] G. M. Nielson, Math. Comput. **40**, 253 (1983).

[98] R. Renka and A. Cline, Rocky Mt. J. Math. **14**, 223 (1984).

[99] Qhull code for convex hull, delaunay triangulation, Voronoi diagram and halfspace intersection about a point, www.qhull.org.

[100] P. Alfeld, Comput. Aided Geom. Des. **1**, 169 (1984).

[101] G. Farin, Comput. Aided Geom. Des. **3**, 83 (1986).

[102] J. D. Hunter, Comput. Sci. Eng. **9**, 90 (2007).

[103] T. A. Caswell, A. Lee, M. Droettboom, E. S. de Andrade, T. Hoffmann, J. Klymak, J. Hunter, E. Firing, D. Stansby, N. Varoquaux, J. H. Nielsen, B. Root, R. May, P. Elson, J. K. Seppänen, D. Dale, J.-J. Lee, D. McDougall, A. Straw, P. Hobson *et al.*, matplotlib/matplotlib: REL: v3.6.0 (2022).

[104] W. Ku, T. Berlijn, and C.-C. Lee, Phys. Rev. Lett. **104**, 216401 (2010).

[105] S. Y. Yang, H. Yang, E. Derunova, S. S. Parkin, B. Yan, and M. N. Ali, Adv. Phys. X **3**, 1414631 (2018).

[106] J. C. Goodrich, D. Borovac, C. K. Tan, and N. Tansu, Sci. Rep. **9**, 5128 (2019).

[107] S.-H. Wei and A. Zunger, Phys. Rev. Lett. **76**, 664 (1996).

[108] J. Wu, W. Walukiewicz, K. M. Yu, J. D. Denlinger, W. Shan, J. W. Ager, A. Kimura, H. F. Tang, and T. F. Kuech, Phys. Rev. B **70**, 115214 (2004).

[109] J. Misiewicz, R. Kudrawiec, and G. Sek, in *Dilute Nitride Semiconductors* (Elsevier, 2005) pp. 279–324.

[110] M. Capizzi, S. Modesti, F. Martelli, and A. Frova, Solid State Commun. **39**, 333 (1981).

[111] A. Strömberg, G. Omanakuttan, Y. Liu, T. Mu, Z. Xu, S. Lourdudoss, and Y.-T. Sun, J. Cryst. Growth **540**, 125623 (2020).

[112] L. Nattermann, A. Beyer, P. Ludewig, T. Hepp, E. Sterzer, and K. Volz, J. Cryst. Growth **463**, 151 (2017).

[113] P. Ludewig, N. Knaub, W. Stolz, and K. Volz, J. Cryst. Growth **370**, 186 (2013).

[114] P. Ludewig, M. Diederich, K. Jandieri, and W. Stolz, J. Cryst. Growth **467**, 61 (2017).

[115] R. B. Lewis, M. Masnadi-Shirazi, and T. Tiedje, Appl. Phys. Lett. **101**, 082112 (2012).

[116] M. Masnadi-Shirazi, R. B. Lewis, V. Bahrami-Yekta, T. Tiedje, M. Chicoine, and P. Servati, J. Appl. Phys. **116**, 223506 (2014).

[117] P. Ludewig, Z. L. Bushell, L. Nattermann, N. Knaub, W. Stolz, and K. Volz, J. Cryst. Growth **396**, 95 (2014).

[118] A. R. Mohmad, F. Bastiman, C. J. Hunter, J. S. Ng, S. J. Sweeney, and J. P. David, Appl. Phys. Lett. **99**, 042107 (2011).

[119] L. A. Cipriano, G. Di Liberto, S. Tosoni, and G. Pacchioni, Nanoscale **12**, 17494 (2020).

[120] https://doi.org/10.17172/NOMAD/2023.02.27-1.

[121] https://bmondal94.github.io/Bandgap-Phase-Diagram/.